

**Determining the activation energy and volume for the onset of plasticity during nanoindentation**

J. K. Mason, A. C. Lund, and C. A. Schuh\*

*Department of Materials Science and Engineering, Massachusetts Institute of Technology, Cambridge, Massachusetts 02139, USA*

(Received 10 August 2005; revised manuscript received 5 October 2005; published 3 February 2006)

Nanoindentation experiments are performed on single crystals of platinum, and the elastic-plastic transition is studied statistically as a function of temperature and indentation rate. The experimental results are consistent with a thermally activated mechanism of incipient plasticity, where higher time-at-temperature under load promotes yield. Using a statistical thermal activation model with a stress-biasing term, the data are analyzed to extract the activation energy, activation volume, and attempt frequency for the rate-limiting event that controls yield. In addition to a full numerical model without significant limiting assumptions, a simple graphical approximation is also developed for quick and reasonable estimation of the activation parameters. Based on these analyses, the onset of plasticity is believed to be associated with a heterogeneous process of dislocation nucleation, with an atomic-scale, low-energy event as the rate limiter.

DOI: [10.1103/PhysRevB.73.054102](https://doi.org/10.1103/PhysRevB.73.054102)

PACS number(s): 62.20.Fe, 61.72.Hh, 68.55.Ac

**I. INTRODUCTION**

During nanoindentation, an indenter tip is brought into contact with a specimen and mechanically loaded with angstrom-level and nanonewton-level control of the displacement and load, respectively. Displacement of the indenter tip initially corresponds to elastic deformation of the surface,<sup>1-16</sup> with the onset of plastic behavior generally observed to coincide with a relaxation event, for example, a displacement excursion during load-controlled nanoindentation.<sup>1-12,14,17-26</sup> This response differs from that measured on macroscopic scales in that the shear stress sustained by the crystal before yield during nanoindentation approaches the order of the theoretical shear strength of the crystal.<sup>3,6-9,11,12,14,15,18,20,22,24-27</sup> Many authors have suggested that this is indicative of a homogeneous dislocation nucleation mechanism,<sup>3,5,10-12,17-21,28,29</sup> which is also reasonable in light of the very low probability of encountering a preexisting dislocation.<sup>5</sup> Recent transmission electron microscopy studies have also correlated the displacement burst with observable dislocation activity,<sup>30,31</sup> although the details of the nucleation event remain elusive.

Dislocation nucleation from a perfect crystal is often assumed to occur when the shear stress beneath the indenter reaches some critical value. For example, Michalske and Houston,<sup>16</sup> as well as Chiu and Ngan,<sup>10</sup> have employed continuum mechanical descriptions of dislocation loop energy<sup>32</sup> to determine the shear stress required to make dislocation nucleation energetically favorable. A number of mechanical nucleation criteria have also been developed based on atomistic considerations, including the  $\Lambda$  criterion<sup>26</sup> and  $N$  criterion.<sup>33</sup> Nucleation-based approaches such as these seem reasonable in light of the discrete nature of incipient plasticity, and are supported by sporadic reports of time and rate dependencies in the experimental literature.<sup>6,10-12,24,29,34</sup> Unfortunately, these studies for the most part neither adequately characterize the time dependence, nor quantitatively relate the time dependence directly to a nucleation mechanism.

In recent work<sup>1,35,36</sup> we have proposed that incipient plasticity be analyzed statistically, to allow direct comparison with the expected statistics of a nucleation event. In a pre-

liminary report we have demonstrated the plausibility of this approach, using variations in loading rate and test temperature to extract values for the activation enthalpy, activation volume, and attempt frequency of incipient plasticity in single crystal platinum.<sup>36</sup> Our purpose in the present paper is to more fully develop both the experimental techniques and analytical tools required for this type of nucleation-based analysis.

**II. EXPERIMENTAL PROCEDURES**

The material used in this study was a 99.999% pure platinum single crystal of (110) orientation, acquired from Goodfellow (Berwin, PA). Platinum was chosen for its favorable oxidation potential at the temperatures of interest, eliminating numerous possible complicating factors from the presence of native oxide.<sup>8,22</sup> Specimens were mechanically polished to 0.1  $\mu\text{m}$ , followed by electropolishing in a supersaturated solution of 100 ml  $\text{H}_2\text{O}$ , 25 ml HCl, and 40 g of NaCl for 2 min at a potential of 4.0 V. When examined with an atomic-force microscope, the sample surface had an rms roughness of less than 1 nm, and asperities or steps appeared only infrequently on the surface.

Nanoindentation was performed using a Hysitron Triboindenter, commercially available from Hysitron, Inc. (Minneapolis, MN), with a Berkovich diamond tip mounted on a low thermal conductivity shaft. An effective tip radius of about 150 nm was determined using standard techniques.<sup>1,2,13,15,16,29,35</sup> Indentations were always placed at least 5  $\mu\text{m}$  apart from one another, and with a constant maximum load of 50  $\mu\text{N}$  for each experiment, the typical indentation depth was below 20 nm. Between indentations, the tip was maintained in contact with the specimen surface at a very low set-point load of 1 or 2  $\mu\text{N}$ ; this prevents issues of jump to contact prior to indentation, as well as artifacts related to indenter momentum during approach.<sup>37,38</sup>

Detailed descriptions of the hardware and procedures we use to perform indentations at elevated temperatures are provided elsewhere,<sup>35,36,39,40</sup> and the details are omitted here for brevity. The equilibrated temperature of the system during

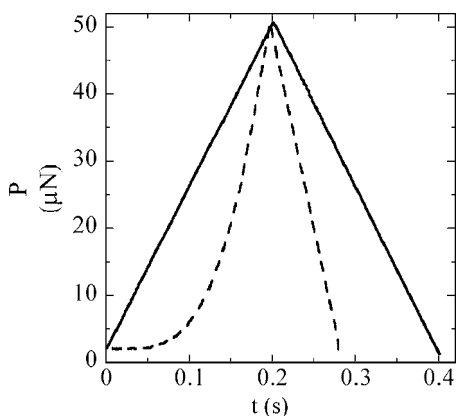


FIG. 1. Examples of typical experimental loading functions (load,  $P$ , vs time,  $t$ ) used in the present study. Most indentations were performed using a constant loading rate (solid line), while some also used a cubic loading function (dashed line).

nanindentation was varied between 25, 100, and 200 °C. The elastic properties of diamond and platinum do not change appreciably in this range,<sup>41–44</sup> so for every set of conditions Poisson’s ratios of 0.07 and 0.39, as well as Young’s moduli of 1140 and 170 GPa, were used for the diamond tip and the platinum specimen, respectively.<sup>45,46</sup>

Two differently shaped loading functions were used during this study, and examples of these are shown in Fig. 1. The majority of tests were performed with a constant loading and unloading rate, corresponding to the solid lines in Fig. 1; the specific value of the loading rate was varied over the range 25–2500  $\mu\text{N s}^{-1}$ . In addition, some experiments were performed with a loading profile represented by the dashed line in Fig. 1, where the load increased as the cube of time and unloading occurred at a constant rate. The motivation for this loading function will be discussed later.

### III. DATA ANALYSIS AND RESULTS

For each indentation, several hundred points on the load-displacement ( $P$ - $h$ ) curve were acquired, and examples of the measured loading response are shown in Fig. 2 at each of the three test temperatures. Although the atomic-scale roughness on indenter tips has recently been shown to lead to modest departures from Hertzian spherical contact theory,<sup>47</sup> the large radius of our indenter tip ( $\rho=150$  nm) and the relatively large characteristic length scale of our indentations (contact radius around 20 nm) render these deviations from the continuum calculations negligible. In line with this argument, we see that the initial portion of the loading curves in Fig. 2 can be well fitted with the expected Hertzian elastic response

$$P = \frac{4}{3} \cdot E_R \cdot \sqrt{\rho h^3}, \quad (1)$$

where  $E_R$  is the reduced modulus of the tip-sample combination, calculated as

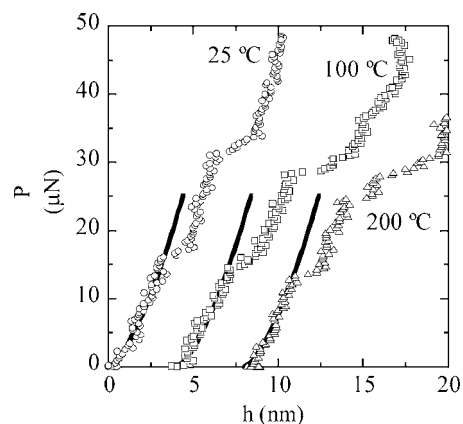


FIG. 2. Representative load-displacement ( $P$ - $h$ ) curves for the loading portion of indentations, obtained at constant loading rate  $\dot{P}=250$   $\mu\text{N/s}$  and various temperatures. Curves for 100 and 200 °C are offset along the  $h$  axis for clarity, and the predictions of Eq. (1) for elastic contact are shown as a solid line for each case.

$$\frac{1}{E_R} = \left( \frac{1-\nu^2}{E} \right)_{\text{diamond}} + \left( \frac{1-\nu^2}{E} \right)_{\text{Pt}}, \quad (2)$$

where  $\nu$  is Poisson’s ratio,  $E$  is Young’s modulus, and the subscripts “diamond” and “Pt” indicate the properties of the indenter and substrate, respectively.<sup>48</sup> The predictions of Eq. (1) are shown as solid lines in Fig. 2, where the deviation of the experiments from the theory can be associated with a “displacement burst,” as is typical in load-controlled nanoindentation experiments. In total, 3062 indentations were performed in this study, and each  $P$ - $h$  curve followed this general behavior. Furthermore, when indentations were performed below the critical burst load, the response was purely elastic (recoverable) and there was no residual impression left at the site of the indentation.

For the purposes of further discussion it is necessary to significantly reduce the full data set, and accordingly we will focus in what follows upon the statistics of the first displacement burst. For each indentation, the first displacement burst was identified using the same procedure. First, each curve was plotted along with the prediction of Eq. (1), and inspected to identify the point of first departure, as shown in Fig. 3(a). Second, the velocity of the indenter tip ( $dh/dt$ ) was calculated and examined relative to that expected for elastic loading based upon the time derivative of Eq. (1) and the experimentally measured load values. For this analysis the measured displacement values were passed through a low-pass filter to reduce high-frequency noise characteristic of the apparatus and operating environment. The output of the procedure appears in Fig. 3(b). The large black circle in this graph corresponds to the point of first departure in the  $P$ - $h$  curve from Fig. 3(a); the first displacement burst corresponds to a momentarily high indenter velocity as the tip “pops” into the specimen surface. The combined use of both the  $P$ - $h$  curve [Fig. 3(a)] and the velocity spike analysis [Fig. 3(b)] provides a robust procedure for uniquely identifying the onset of plasticity.

Some characteristic statistical distributions for the first displacement burst are shown graphically in Fig. 4, for in-

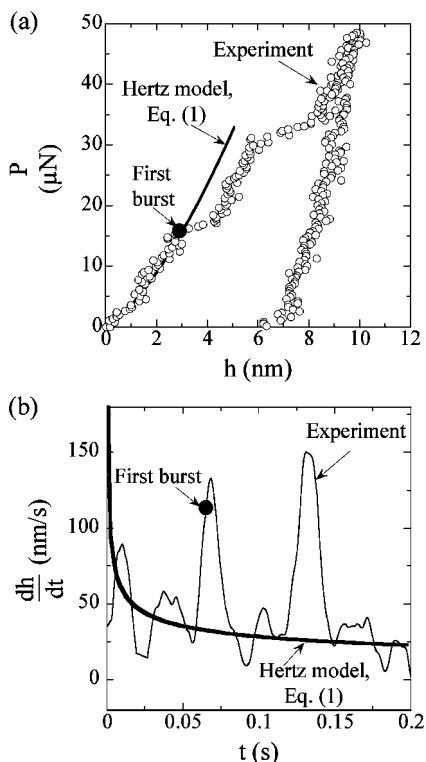


FIG. 3. Procedure for identifying the first displacement burst during nanoindentation of (110)-oriented platinum at 25 °C with a constant loading rate of 250  $\mu\text{N s}^{-1}$ . The first burst (denoted by a large black circle) is associated with the first departure from the Hertzian elastic contact theory [Eq. (1)] in the  $P$ - $h$  curve (a), as well as a measurable velocity spike (b).

dentations performed with constant loading rates on (110)-oriented platinum. Each curve in these graphs is an experimentally determined cumulative fraction distribution of the first displacement burst; the horizontal axes represent the applied indenter load at the burst point, while the vertical axes represent the fraction of indentations that yielded at or below the given load. Cumulative statistics are superior to histograms for this purpose, because no subjective binning and associated lost resolution are involved. Figure 4(a) illustrates the effect of temperature at constant loading rate, while Fig. 4(b) shows the effect of loading rate at a constant test temperature. These data typify a trend present throughout all of our tests, in which the first burst occurs at lower loads when temperature is increased or when rate is decreased; plasticity is promoted by higher time at temperature.

#### IV. ANALYTICAL

The data shown in Fig. 4 demonstrate a clear time and temperature dependence to incipient plasticity. While time dependencies have been reported in some prior studies at ambient temperature,<sup>1,6,10-12,24,29,34</sup> the present data set is the first to simultaneously catalog both time and temperature dependencies. The fact that higher temperatures and lower rates promote the first displacement burst speaks, in our opinion, to a stress-biased, thermally activated yield mechanism. We

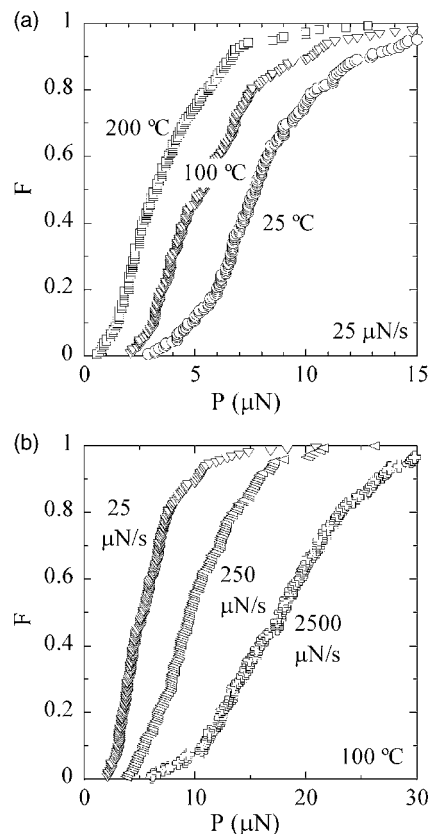


FIG. 4. Examples of the statistical data acquired for the first displacement burst during nanoindentation of (110)-oriented platinum. The cumulative fraction,  $F$ , of experimental loads,  $P$ , at the burst point are plotted for many indentations performed with the same experimental conditions. Part (a) shows the effect of test temperature for sets of indentations at a constant loading rate  $\dot{P} = 25 \mu\text{N/s}$ , while part (b) shows the effect of rate at a constant temperature  $T = 100 \text{ }^\circ\text{C}$ .

imagine that there is a single local, kinetically limiting process that takes place under the indenter (for example, the nucleation of a dislocation), which requires an activation enthalpy. This energy barrier could be reduced through the mechanical work of indentation, may be overcome by an appropriate thermal fluctuation, or may be surpassed by a combination of both thermal and mechanical energy. Statistically, the process may be described by a rate equation of the form

$$\dot{n} = \eta \exp\left(-\frac{\varepsilon - \sigma V}{kT}\right), \quad (3)$$

where  $\dot{n}$  is the local rate at which the critical event occurs per unit volume of material,  $\varepsilon - \sigma V$  is the activation energy for the reaction,  $kT$  is the average available thermal energy, and  $\eta$  is a pre-exponential frequency factor. For the process under consideration, the activation energy is separated into a term characterizing the activation enthalpy, represented by  $\varepsilon$ , and a term capturing the stress bias, represented by  $\sigma V$ , where  $\sigma$  is the biasing stress over the activation volume  $V$ . The separation of the activation energy into individual com-

ponents is made more transparent by expressing the function in the form

$$\dot{n} = \eta \exp\left(-\frac{\varepsilon}{kT}\right) \exp\left(\frac{\sigma V}{kT}\right), \quad (4)$$

where the first exponential term gives the probability per attempt of a yield event in a perfect, stress-free crystal, and the second makes explicit the exponential dependence of the rate of displacement bursts on applied stress.

Equation (4) gives a displacement burst rate for a volume element of material under a constant stress state, but the stress field under a nanoindentation is a strong function of position. Formally, the global rate at which displacement bursts would occur ( $\dot{N}$ ) would be found by integrating over the volume of the indented material near the contact region ( $\Omega$ )

$$\dot{N} = \eta \cdot \exp\left(-\frac{\varepsilon}{kT}\right) \cdot \int \int \int_{\Omega} \exp\left(\frac{\sigma V}{kT}\right) d\Omega. \quad (5)$$

Full evaluation of the above integral would require not only that we know which terms from the full stress tensor constitute  $\sigma$ , but also that we know how stress changes with position beneath the indenter.

For a series of nominally identical indentations such as we have performed in our experiments, the ultimate link between Eq. (5) and the cumulative fraction function,  $F(t)$ , for the statistics of the first burst is derived as follows. The rate of change of  $F(t)$  is necessarily proportional to the number of unyielded samples remaining, and to the rate at which one of those remaining samples displays the onset of plasticity

$$\dot{F}(t) = [1 - F(t)]\dot{N}(t). \quad (6)$$

Integrating this equation and discarding the physically unreasonable solution yields

$$F(t) = 1 - \exp\left(-\int_0^t \dot{N}(t') dt'\right). \quad (7)$$

With a relationship between indentation load and time,  $F(t)$  is readily converted to cumulative load statistics [ $F(P)$ ] such as we measure experimentally (cf. Fig. 4).

Equations (5) and (7) represent a general statistical framework for the analysis of displacement bursts during nanoindentation, provided the integral in Eq. (5) can be evaluated. In the following subsections we discuss two separate approaches to this problem. The first of these requires simplifying assumptions but admits an analytical solution, while the second resorts to numerical evaluation without significant assumptions. Later we compare these two approaches, and discuss extensions and modifications to the model that may yield physical insight into incipient plasticity.

### A. First-order analytical solution

The current understanding of incipient plasticity during nanoindentation is that the displacement burst corresponds to the nucleation of at least one dislocation, which occurs pri-

marily due to the action of a shear stress,  $\tau$ . For the present analysis, therefore, we will approximate the stress bias as equal to the maximum shear stress beneath the indenter, given within the Hertzian contact framework as<sup>49</sup>

$$\sigma \equiv \tau_{\max} = \frac{0.47}{\pi} \cdot \left(\frac{4E_R}{3\rho}\right)^{2/3} P^{1/3}. \quad (8)$$

Equation (8) describes the stress at a single point beneath the indenter; here we assume that the biasing stress scales with this value, such that  $\sigma$  is independent of position and the exponential in the integral of Eq. (5) becomes a constant with respect to position. Evaluation of Eq. (5) then requires only an expression for the sampling volume,  $\Omega$ , which can also be described in the Hertzian framework by assuming that  $\Omega$  scales with the cube of the contact radius,  $a$

$$\Omega \approx Ka^3 = K\left(\frac{3P\rho}{4E_R}\right), \quad (9)$$

where  $K$  is a proportionality constant which we take to be of order  $\sim \pi$ .

Given the rate of displacement burst events of Eq. (5), we now require a description of the loading function applied to the indenter tip to introduce time and allow the evaluation of Eq. (7). For the moment we assume a constant loading rate,  $\dot{P}$ , which was the most commonly used loading profile in our experiments

$$P = \dot{P} \cdot t. \quad (10)$$

Combining Eqs. (5) and (7)–(10) and evaluating then yields the cumulative fraction function

$$F(P) = 1 - \exp\left\{-\frac{9K\rho\eta}{4E_R\dot{P}\alpha^6} \exp\left(-\frac{\varepsilon}{kT}\right) [120 + \exp(P^{1/3}\alpha) \cdot (P^{5/3}\alpha^5 - 5P^{4/3}\alpha^4 + 20P\alpha^3 - 60P^{2/3}\alpha^2 + 120P^{1/3}\alpha - 120)]\right\}. \quad (11)$$

Here the parameter  $\alpha$  is a collection of time-independent terms, given by

$$\alpha \equiv \frac{0.47}{\pi} \left(\frac{4E_R}{3\rho}\right)^{2/3} \frac{V}{kT}. \quad (12)$$

### B. Second-order numerical solution

While the use of  $\tau_{\max}$  provides a soluble, first-order approximation to the integral in Eq. (5), it implicitly assumes the nucleation event to occur at a specific position beneath the indenter; this solution therefore neglects the fact that there is a non-negligible shear field of finite extent beneath the spherical indenter. Within the Hertzian framework, the entire stress field is given by<sup>49</sup>

$$\begin{aligned} \sigma_{rr}(r,z) = & \frac{3}{2} \frac{P}{\pi a^2} \left\{ \frac{1-2\nu a^2}{3} \frac{1}{r^2} \left[ 1 - \left( \frac{z}{u^{1/2}} \right)^3 \right] \right. \\ & + \left( \frac{z}{u^{1/2}} \right)^3 \frac{a^2 u}{u^2 + a^2 z^2} + \frac{z}{u^{1/2}} \left[ u \frac{1-\nu}{a^2 + u} \right. \\ & \left. \left. + (1+\nu) \frac{u^{1/2}}{a} \tan^{-1} \left( \frac{a}{u^{1/2}} \right) - 2 \right] \right\}, \end{aligned} \quad (13)$$

$$\begin{aligned} \sigma_{\theta\theta}(r,z) = & -\frac{3}{2} \frac{P}{\pi a^2} \left\{ \frac{1-2\nu a^2}{3} \frac{1}{r^2} \left[ 1 - \left( \frac{z}{u^{1/2}} \right)^3 \right] + \frac{z}{u^{1/2}} \right. \\ & \left. \times \left[ 2\nu + u \frac{1-\nu}{a^2 + u} - (1+\nu) \frac{u^{1/2}}{a} \tan^{-1} \left( \frac{a}{u^{1/2}} \right) \right] \right\}, \end{aligned} \quad (14)$$

$$\sigma_{zz}(r,z) = -\frac{3}{2} \frac{P}{\pi a^2} \left( \frac{z}{u^{1/2}} \right)^3 \left( \frac{a^2 u}{u^2 + a^2 z^2} \right), \quad (15)$$

$$\tau_{rz}(r,z) = -\frac{3}{2} \frac{P}{\pi a^2} \left( \frac{r z^2}{u^2 + a^2 z^2} \right) \left( \frac{a^2 u^{1/2}}{a^2 + u} \right). \quad (16)$$

These equations use cylindrical coordinates  $(r, \theta, z)$  originating from the center point of the tip-specimen contact, with  $z$  measuring depth into the half volume from the surface. Here  $\nu$  is Poisson's ratio of the specimen and  $u$  is

$$u = \frac{1}{2} [(r^2 + z^2 - a^2) + \sqrt{(r^2 + z^2 - a^2)^2 + 4a^2 z^2}]. \quad (17)$$

At a given point in the solid, the maximum shear stress is then

$$\pi(r,z) = \sqrt{\left( \frac{(\sigma_{rr} - \sigma_{zz})}{2} \right)^2 + \tau_{rz}^2}. \quad (18)$$

Equation (18) can be introduced into Eq. (5) to yield

$$\dot{N} = \eta \cdot \exp\left(-\frac{\varepsilon}{kT}\right) \cdot \int_0^{4a} \int_0^{3a} \exp\left(\frac{\pi(r,z)V}{kT}\right) \cdot 2\pi r \cdot dr \cdot dz, \quad (19)$$

where the volume integral has been cast into cylindrical coordinates. This integral is unbounded when performed over an infinite volume, so finite limits have been assigned defining the relevant contact zone. The shear stress and pressure at the boundary of this zone reach only about one tenth the maximum values contained within it; it is reasonable to neglect nucleation events outside this volume due to the extremely low stress bias. Although the choice of integration limits is somewhat arbitrary, we have confirmed the suitability of those given in Eq. (19) by integrating over regions with volumes ranging from  $10 \cdot a^3$  to more than  $250 \cdot a^3$ , without observing any meaningful variation in the results. This range of volumes corresponds to boundary values of the shear stress (and pressure) ranging from one half to one twentieth of the maximum values.

Due to the complexity of the stress bias in Eq. (19), analytical solution of the volume integral is not straightforward. The full connection to experimental burst statistics is best

made through recourse to numerical evaluation of the integrals in Eqs. (19) and (7).

## V. EXTRACTION OF ACTIVATION PARAMETERS FROM EXPERIMENTAL DATA

In this section we use the mathematics outlined above to extract specific values of the activation parameters from the experimental data of Fig. 4. In the following two subsections we examine the first- and second-order models in turn, and report the activation parameters obtained. In subsequent discussion we compare the results obtained with these two models, and consider their physical implications.

### A. First-order analysis

Equation (11) expresses the expected form of the cumulative distribution functions for the first displacement burst, and varies with test temperature and applied loading rate; it can be compared directly with the experimental data in the form shown in Fig. 4, and in what follows we fit these data with Eq. (11), treating the values of  $\eta$ ,  $\varepsilon$ , and  $V$  as unknown adjustable parameters. In the interest of simplicity and utility, we recast Eq. (11) into the following form that isolates the dominant load dependence

$$\ln \left[ \ln \left( \frac{1}{1-F(P)} \right) \right] = \alpha P^{1/3} + \beta, \quad (20)$$

where the parameter  $\beta$  is of weak  $P$  dependence as compared to the first term on the right-hand side of Eq. (20), and is given by

$$\begin{aligned} \beta = \ln \left\{ \frac{9K\rho\eta}{4E_R \dot{P} \alpha^6} \exp\left(-\frac{\varepsilon}{kT}\right) [120 \exp(-P^{1/3}\alpha) + P^{5/3}\alpha^5 \right. \\ \left. - 5P^{4/3}\alpha^4 + 20P\alpha^3 - 60P^{2/3}\alpha^2 + 120P^{1/3}\alpha - 120] \right\}. \end{aligned} \quad (21)$$

For experiments performed at a constant loading rate and temperature, Eq. (20) is particularly valuable for extraction of the constants  $\alpha$  and  $\beta$  from experimental data. By plotting  $\ln(\ln(1-F)^{-1})$  versus  $P^{1/3}$ , experimental data fall onto roughly linear trendlines that are easily fitted with the method of least squares; this is illustrated in Fig. 5 for data sets acquired at room temperature at three different loading rates. With  $\alpha$  the measured slope of these curves, Eq. (12) is inverted to yield the activation volume  $V$

$$V = \frac{\pi}{0.47} \left( \frac{3\rho}{4E_R} \right)^{2/3} kT \cdot \alpha. \quad (22)$$

The above analysis has been performed for 11 different combinations of temperature and loading rate (including those shown in Fig. 4), for indentations performed on the (110) surface of platinum. Averaging the values of the activation volume for each of the eleven sets of data yields  $V=9.7 \text{ \AA}^3$ , with a standard deviation of only  $1.9 \text{ \AA}^3$ .

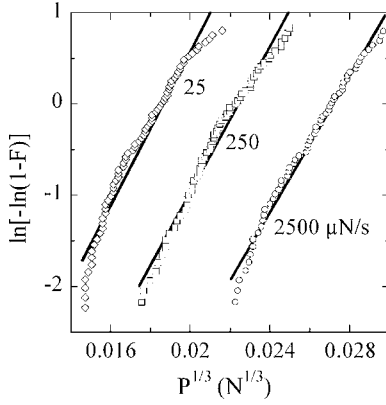


FIG. 5. Example of the linear least-squares procedure used to extract the activation volume from experimental data by the first-order analysis, omitting less-reliable data near the tails of the curves. Experimental data like those from Fig. 4(b) (but at  $T = 25^\circ\text{C}$ ) are plotted according to the form of Eq. (20), and the solid lines are the best fits of that equation to the data.

The activation enthalpy can also be extracted from experimental data using a similar linearization approach. In this case we write Eq. (11) in a form that isolates  $\varepsilon$

$$P^{1/3} = \gamma k T + \frac{\pi}{0.47} \left( \frac{3\rho}{4E_R} \right)^{2/3} \frac{\varepsilon}{V}, \quad (23)$$

where  $\gamma$  is a complex function whose form is not of particular importance, but which incorporates a dependence on both  $F(P)$  and  $\dot{P}$ . The temperature dependence of  $\gamma$  is weak compared to the linear  $T$  term multiplying it in Eq. (23), and its pressure dependence is weak compared with that on the left-hand side of the expression. Equation (23) can be used to extract  $\varepsilon$  from experimental data in the following straightforward way. First, cumulative fraction functions are identified which differ in only the temperature at which they were performed, with loading rate constant among the selected data. Second, loads corresponding to a constant chosen value of  $F(P)$  are identified; for example, the median load of each distribution [the value of  $P$  at which  $F(P)=0.5$ ]. Having fixed both  $\dot{P}$  and  $F(P)$ , a plot of  $P^{1/3}$  vs  $T$  is linear, with a slope  $\gamma k$  and intercept proportional to  $\varepsilon/V$ .

Examples of the above construction are shown in Fig. 6, for data acquired on (110)-oriented platinum at a loading rate of  $25 \mu\text{N s}^{-1}$ . Here we have plotted the data for the median burst load as well as the values at the 30th and 70th percentile of the cumulative distribution. Linear least-squares fitting of Fig. 6 gives, via the value of the  $y$  intercept, a numerical evaluation of the ratio  $\varepsilon/V$ . Earlier in this section we extracted  $V$  from a separate analysis, and introducing this value allows us to determine the activation enthalpy  $\varepsilon \approx 0.34 \pm 0.03 \text{ eV}$  when averaging over all of our experimental data for indentation of (110)-oriented platinum.

With values for  $\varepsilon$  and  $V$  derived from the above fitting procedures, the only remaining unknown is the attempt frequency,  $\eta$ , which can easily be calculated from any individual data set by assessing the value of the intercept,  $\beta$ , and inverting Eq. (21). Averaging over all of the data sets then

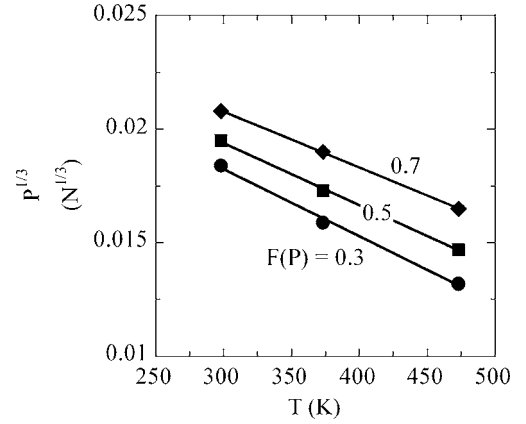


FIG. 6. Graphical construction of Eq. (23), used to extract the activation enthalpy for the first displacement burst. The points show experimental data obtained at  $\dot{P} = 25 \mu\text{N/s}$  for three different temperatures, and the solid lines are the best fits of Eq. (23). The three trendlines shown converge to a common  $y$  intercept ( $\sim 0.0276 \pm 0.005 \text{ N}^{1/3}$ ) at  $T=0$ , which is proportional to the activation enthalpy via Eq. (23).

gives a best-fit value of  $\eta$ ; because  $\eta$  is a pre-exponential constant the averaging is best performed on logarithmic scales, i.e.,  $\bar{\eta} = \exp(M^{-1} \sum \ln \eta)$ , where the summation runs over all  $M$  data sets. This procedure yielded an average attempt frequency of  $\bar{\eta} \approx 7 \times 10^{25} \text{ s}^{-1} \text{ m}^{-3}$  for the data from (110) platinum.

## B. Second-order analysis

For the second-order analysis encapsulated in Eqs. (7) and (19), there is no simple graphical construction with which to fit the model to data. Instead, a full numerical solution to the equations must be calculated for trial values of the parameters  $\varepsilon$ ,  $V$  and  $\eta$ . Here we have used an iterative fitting procedure to minimize the square error on  $F(P)$  and optimize the values of these parameters for best fit to the data for (110)-oriented platinum. Rather than fitting individual sets of data, we have performed a simultaneous fit to all 11 sets of data shown in Fig. 7. These graphs incorporate the data from Fig. 4, as well as additional combinations of temperature and loading rate.

The results of the numerical fitting procedure are shown by the solid lines atop the experimental data in Fig. 7. From these graphs we see that our statistical interpretation of incipient plasticity captures the proper sigmoidal trend of the curves, as well as the shifts in the cumulative distributions that arise from either loading rate [Figs. 7(a)–7(c)] or temperature [Fig. 7(d)] variations. The fit is generally quite satisfactory, especially at the higher test temperatures. From this analysis we obtain an activation volume of  $V \approx 10.2 \text{ \AA}^3$ , an activation enthalpy of  $\varepsilon \approx 0.28 \text{ eV}$ , and an attempt frequency of  $\eta \approx 1.8 \times 10^{25} \text{ s}^{-1} \text{ m}^{-3}$ .

## C. Robustness of the analysis methods

In the first two rows of Table I we have collected the best-fit values of activation enthalpy, activation volume, and

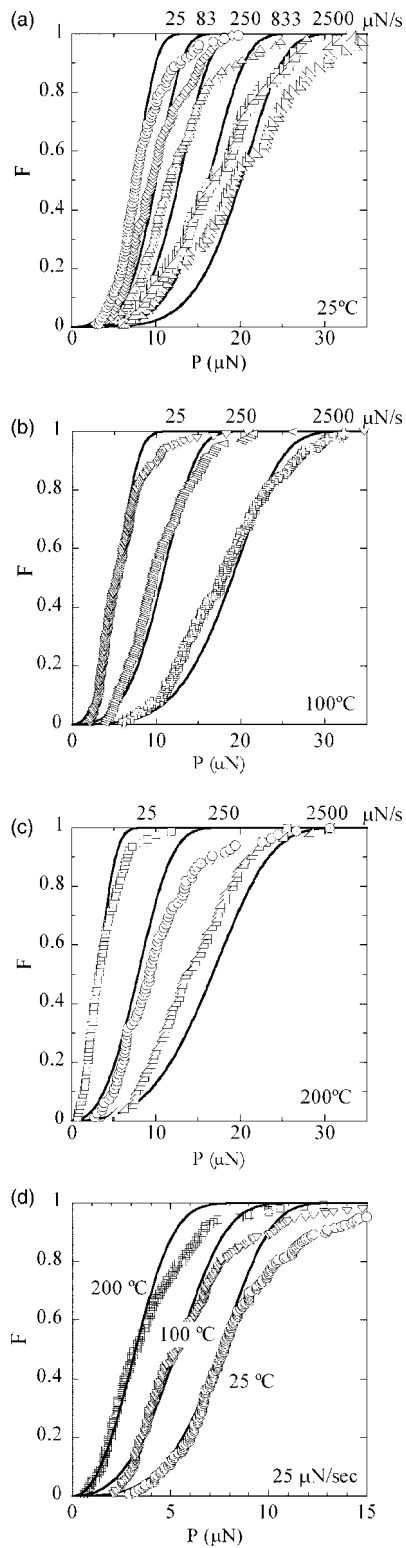


FIG. 7. All of the experimental data collected in this study for constant loading rate indentations on (110) platinum are shown here as symbols, with the fit obtained using the second-order shear-biased model [Eq. (3), ( $\sigma = \tau$ )] shown as solid lines. The goodness of the fit with respect to loading rate variations can be seen in (a)–(c) at temperatures of 25, 100, and 200 °C, respectively. In (d) all the data sets obtained at 25  $\mu\text{N/s}$  are displayed to better illustrate the subtle temperature effects captured by the model.

attempt frequency as obtained from both the first- and second-order models described above. It is clear that the extracted parameters are quite similar, indicating that the additional mathematical complexity of the second-order model does not fundamentally change the results. In order to probe the robustness of the analysis methods, we have also performed additional experiments with a nonlinear loading profile (cf. Fig. 1). In this case the applied load was increased as the cube of time

$$P = At^3. \quad (24)$$

The motivation for this functional form derives from the Hertzian model of Eq. (8), which requires a cubic loading profile in order to maintain a constant rate of shear stress increase. This choice of load function is preferred for mathematical simplicity if one intends to use the first-order approximation described in Sec. V A, as detailed in Appendix A. For the present purposes, however, we are interested solely in the predictive ability of the model for an independent set of data acquired with a different loading condition.

Figure 8 shows three sets of data acquired at room temperature using three different cubic loading profiles [i.e., three different values of  $A$  in Eq. (24)]. Shown for comparison are the predictions of our second-order numerical model incorporating the time dependence of Eq. (24) rather than a constant loading rate, using the activation parameters from row two of Table I as inputs. Clearly, with no fitting parameters, the model captures the trends seen in the data, and is a good quantitative match to the experiments as well, with a coefficient of determination  $R^2 = 0.94$ . This result verifies that the model, once calibrated, can capture events occurring under somewhat different test conditions without the need for adjustable parameters.

## VI. DISCUSSION

In the prior sections we have demonstrated that a thermally activated, stress-biased mechanism can account for the observed rate and temperature dependencies of incipient plasticity. Both first- and second-order analyses give roughly the same activation parameters, and in principle these parameters should reflect the nature of the rate-limiting process that controls plastic yield at the nanoscale. Although we cannot observe atomic-level mechanistic details, the mathematical framework outlined above can be used to test many existing theories about the nature of incipient plasticity. In what follows, we will examine several such theories in turn, introducing appropriate modifications to our model where necessary, and quantitatively evaluating each proposed yield mechanism.

### A. Homogeneous dislocation nucleation

It has been widely speculated that the first displacement burst during nanoindentation is associated with a homogeneous dislocation nucleation mechanism,<sup>3,5,10–12,17–21,28,29</sup> a notion that has been supported by atomistic simulations of nanoindentation on defect-free, clean metal surfaces.<sup>18–20,28,50–54</sup> According to this picture, the first burst

TABLE I. Activation parameters for incipient plasticity, extracted by fitting statistical models to the experimental data. All rows are for fitting to the experimental data from (110)-oriented platinum except where noted.

Model used	Eqs.	$\varepsilon$ (eV)	$V$ ( $\text{\AA}^3$ )	$\eta$ ( $10^{25} \text{ m}^{-3} \text{ s}^{-1}$ )	$R^2$
First order, shear bias ( $\sigma = \tau_{\text{max}}$ )	(3)	0.34	9.7	7	0.72
Second order, shear bias ( $\sigma = \tau$ )	(3)	0.28	10.2	2	0.89
Second order, shear plus pressure	(25)	0.29	18.9	2	0.91
Second order, vacancy migration	(27)	0.11	65.0	0.08	0.36
Second order, shear bias ( $\sigma = \tau$ ) for the (111) surface	(3)	0.34	9.9	13	0.82

would be controlled by a cooperative process of atomic motion to form a critical-sized dislocation loop. From a continuum dislocation-mechanics perspective, at applied stresses below the theoretical shear strength the critical loop would comprise many atomic volumes.<sup>10,16,29,32,55,56</sup> Similarly, the activation enthalpy should be reflective of many bond breakages, on the order of several eV and significantly out of the range of thermal energy fluctuations.

The statistical model we have presented earlier is reasonably appropriate for the case of homogeneous dislocation nucleation, as the stress bias for such a process is expected to be dominated by shear terms. Based on this model, the experimental data suggest an activation volume somewhat smaller than the cubed Burger's vector ( $V \approx 0.5 \text{ b}^3$ ), and an activation enthalpy ( $\varepsilon \approx 0.28 \text{ eV}$ ) below that for point defect migration in platinum ( $\sim 1.3 \text{ eV}$ ).<sup>57</sup> These values are much lower than would be expected for a critical-sized homogeneous dislocation loop at stresses below the ideal shear strength, and more importantly permit thermal energy fluctuations to activate the nucleation process, as is generally considered inconsistent with homogeneous nucleation.<sup>58-60</sup> Although some of our most extreme measured yield points do correspond to shear stresses near the ideal strength of platinum (given as  $\sim 5.3 \text{ GPa}$  by Pokluda *et al.*<sup>61</sup>), the vast

majority of the data correspond to much lower applied stress levels, in many cases less than half of the ideal strength. For these conditions the activation enthalpy and volume for homogeneous dislocation loop nucleation are both expected to be much higher than the values we have measured.<sup>58,59</sup> Accordingly, the present experimental results appear inconsistent with a process of homogeneous dislocation nucleation.

There are several possible explanations for the apparent discrepancy between experiments and the homogeneous dislocation nucleation mechanism described above. For example, our analysis assumed a relatively simple form for the activation energy of loop nucleation, and refinements to the form of Eq. (3) are certainly possible. Khantha, Pope, and Vitek<sup>56,62,63</sup> have discussed the issue of dislocation nucleation in a stressed solid, and pointed out that the process may be impacted by the presence of a finite population of subcritical loops. Those authors developed a model in which the local elastic modulus is reduced by virtue of these subcritical loops, which in turn lowers the enthalpy barrier to dislocation nucleation. In principle, this amounts to incorporating a stress and temperature dependence into  $\varepsilon$ , rather than treating it as a constant as we have done. In order to examine the effects of this modification to  $\varepsilon$ , we have numerically evaluated the model of Khantha and co-workers for our experimental conditions, and we find that it predicts extremely low stresses to nucleate a critical dislocation loop (more than a factor of 2 below our median applied stress levels). It seems that without some modifications, this model cannot be properly compared with our data. A philosophically similar model has been proposed by Sun, Hazzledine, and Hirsch,<sup>64</sup> in which subcritical loops in the stressed volume influence nucleation through their image stress fields,  $\tau_{\text{im}}$ . In this case the activation enthalpy  $\varepsilon$  may be taken as constant, but an additional term involving the activation volume ( $\tau_{\text{im}}V$ ) would be included in Eq. (3). The implementation of this model within our current framework is not straightforward, however, because it assumes a voluminous, uniformly stressed material that is inconsistent with the indentation geometry.

Both of the models described above represent adjustments to the form of Eq. (3), and certainly many further models can be envisioned that incorporate additional dependencies into the activation energy. It is important to note that such modifications do not change the basic physical viewpoint of our approach. As an example to illustrate this point, we consider a third potential modification to the form of Eq. (3), which

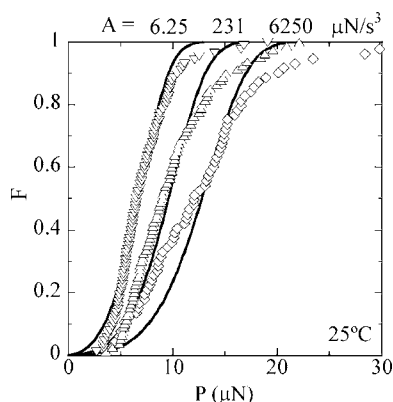


FIG. 8. Data from experiments performed using a cubic loading function [ $P=At^3$ , Eq. (24)] are shown by the symbols. The experimental data are well predicted without adjustable parameters using the second-order shear-biased model, shown here as solid lines. Evaluation of the model takes as input the activation parameters extracted earlier from the constant loading rate data (Table I, row 2).

can be directly incorporated into the analysis: pressure dependence of the nucleation enthalpy. This adaptation is motivated by the work of Jung,<sup>65</sup> who calculated the increase in line energy of a dislocation under pressure; this concept has recently been applied to heterogeneous loop nucleation from grain boundary sources.<sup>66,67</sup> To incorporate this effect into our model, Eq. (3) is adapted as

$$\dot{n} = \eta \exp\left(-\frac{(1 + \xi\sigma_P)\varepsilon - \tau v}{kT}\right), \quad (25)$$

where the hydrostatic pressure is given by

$$\sigma_P = -\frac{1}{3}(\sigma_{rr} + \sigma_{zz} + \sigma_{\theta\theta}) \quad (26)$$

and the magnitude of the pressure effect is measured by the multiplicative factor  $\xi$ . Based upon the model in Ref. 65, the value of  $\xi$  is estimated as 0.17 GPa<sup>-1</sup> for platinum. Carrying Eq. (25) through our earlier derivation of the second-order numerical analysis, the experimental data can be fitted in much the same way, but inclusive of the complex pressure field under the indenter [Eqs. (13)–(15)]. Least-squares fitting of the data with this model yields activation parameters that are given in the third row of Table I.

We can see from the results in Table I that the inclusion of a pressure effect has a few relatively minor consequences for the interpretation of our nanoindentation experiments (compare rows 2 and 3). First, the fit of model to data marginally improves when the pressure dependence is included, as evidenced through the increase in  $R^2$ . Second, the added pressure dependence gives a larger activation volume, quite close to the atomic volume of platinum. This is justifiable on the basis that pressure effectively increases the activation enthalpy, and the magnitude of the stress-biasing term must accordingly increase to overcome the enthalpy barrier and nucleate dislocations. Of course, the value of  $\xi$  used here was based on a continuum description of dislocations, while the event we are concerned with seems rather small for such an approach. Nonetheless, the simple pressure dependence of Eq. (25) need not be associated with any particular mechanism, and the magnitude of  $\xi$  is physically appropriate. The main point captured by the parameters in Table I is that a reasonable pressure dependence does not substantially change the size or energy of the rate-limiting process behind incipient plasticity, and these parameters remain much smaller than expected for homogeneous dislocation nucleation.

Having addressed possible variations on the form of the activation energy for incipient plasticity, we now consider an alternative explanation for the magnitudes of the experimentally obtained activation enthalpy and volume: perhaps the very small activation parameters we have measured reflect a near-atomic size volume for the homogeneous dislocation loop's critical size. For example, Zuo, Ngan, and Zheng<sup>17</sup> have used atomistic simulations to show that dislocation nucleation events can be traced back to specific initial thermal fluctuation sites that are essentially one atom in size. Wo, Zuo, and Ngan<sup>68</sup> have proposed that this may be the situation beneath a nanoindenter, and that the activation volume measured from experiment may correspond to the initial

thermal fluctuation site. However, studies based on the continuum description of dislocations have shown that thermal fluctuations only participate in homogeneous loop nucleation at stresses very close to the theoretical shear strength.<sup>58,59</sup> A similar conclusion can be drawn from more sophisticated nudged elastic band calculations<sup>69</sup> which have very recently been used to identify the saddle-point configuration for dislocation nucleation. As mentioned earlier, in the present experiments the applied shear stresses are mostly well below the theoretical strength of platinum, so it is very difficult to envision a critical loop diameter on the order of a single atomic volume.

On balance, in light of the above discussion, it seems that the homogeneous nucleation of a dislocation under our experimental conditions would require significantly higher activation enthalpy and volume than we have extracted from our nanoindentation data, and less sensitivity to temperature and rate than we see experimentally. Accordingly, we favor a heterogeneous mechanism as rate limiting for the onset of plasticity during nanoindentation. Such mechanisms are analyzed further below.

### B. Point defect mechanisms

The magnitudes of  $\varepsilon$  and  $V$  extracted from our experiments are both reflective of an atomic-scale event, so it is appealing to imagine a point defect-related process as the rate limiter for plastic yield. Several authors have made such proposals in the past. For example, Farber *et al.*<sup>70–73</sup> used microindentation experiments in combination with constitutive flow laws, and proposed that deformation at small indentation sizes was limited by point defect activity in nonmetallic compounds; they did not explicitly study incipient plasticity. Ngan and co-workers<sup>10,74</sup> proposed that vacancy migration could limit deformation by enabling the climb of a subcritical dislocation loop, allowing it to reach the critical size for unrestricted propagation. Although self-diffusion is slow at ambient temperatures, these authors have argued that the large pressure gradient under a nanoindenter would significantly increase diffusivity. Even without migration of vacancies, it seems possible that dislocation nucleation could occur preferentially at a vacancy or a cluster of vacancies, as envisioned in the 1950 work of Seitz.<sup>75</sup>

In the present case, the equilibrium vacancy concentration for platinum is much too low to justify a picture involving preexisting vacancies beneath the indenter.<sup>57</sup> At the test temperatures we have employed, the probability of encountering a preexisting equilibrium vacancy beneath a  $\sim 4$ -nm-deep nanoindentation would be on the order of  $\sim 10^{-6}$ . Accordingly, the only possible scenario in which preexisting vacancies might play a role in incipient plasticity is one in which the specimen is out of equilibrium to a significant degree. In the present case, this seems plausible, as a single crystal offers very few sinks for vacancy annihilation during cooling to room temperature. If we were to assume a quenched-in nonequilibrium vacancy density corresponding to a temperature of  $\sim 2/3 \cdot T_m$  (with  $T_m$  the melting temperature), the likelihood of encountering a vacancy increases substantially, to the point where every indentation would see a handful of vacancies.<sup>57</sup>

Proceeding on the assumption that vacancies are present beneath each indentation, we can evaluate the vacancy migration-limited mechanism in the following way. The bias in this case is the hydrostatic stress gradient, which drives vacancy migration towards points of higher pressure in order to relieve compressive stresses. Only the magnitude of the pressure gradient,  $|\nabla\sigma_p|$ , will bias the migration of a vacancy, and for a substitutional diffusion mechanism this bias acts over a distance roughly equal to the magnitude of the Burgers vector,  $b$ . If a migration event on this scale controls the nucleation of a dislocation, we can write

$$\dot{n} = \eta \exp\left(-\frac{\varepsilon - |\nabla\sigma_p|bV}{kT}\right). \quad (27)$$

This expression is easily introduced into our second-order numerical analysis, with  $|\nabla\sigma_p|$  calculated from Eqs. (13)–(15) and (23). The values we have obtained from this analysis are given in row 4 of Table I, but as evidenced by the low  $R^2$  value we could not achieve a satisfactory fit. No combination of activation parameters could reproduce the qualitative form of the experimental results. Furthermore, the extracted values of  $V$  and  $\varepsilon$  are out of line with the expectations for vacancy migration, for which  $V$  should be very close to an atomic volume, and the activation enthalpy  $\varepsilon$  would be expected to match that for vacancy migration in platinum (1.43 eV).<sup>57</sup> This result is somewhat expected, as the mechanical bias due to the pressure gradient does not significantly increase diffusivity and vacancy migration remains very slow at our test temperatures. The above analysis has also neglected the slight pressure dependence of  $\varepsilon$ , which would tend to further slow diffusion. We have included this effect in another variation of our model as well, but the resulting fit is even poorer and we omit the details here.

In light of the above discussion, we consider any mechanism based on vacancy diffusion to be an unlikely candidate as the rate limiter for incipient plasticity. However, it remains a possibility that a preexisting vacancy could act as a heterogeneous nucleation site for dislocations. This situation is reasonably well modeled by the shear-biased analyses presented above, and provides an appealing explanation for the low activation parameters we have obtained. Unfortunately, we know of no prior models for the dissociation of a single vacancy into a shear loop; the traditional view as espoused by Seitz<sup>75</sup> and others<sup>76</sup> generally assumes a cluster of vacancies. It seems possible that a single vacancy could serve the same function in the highly stressed volume under a nanoindenter, and this could be a fruitful avenue for future atomistic studies. In any case, it is important to remember that such a vacancy-based mechanism would require a quenched-in elevated vacancy concentration.

One final hypothesis can be advanced for a point-defect related mechanism of incipient plasticity. Even with 99.999% pure metal, as used in this study, the density of impurity atoms is such that they cannot be avoided even at very small indentation depths. The effect of impurities on the nucleation of dislocations has not, to our knowledge, been studied in sufficient detail to offer a quantitative model here. However, the activation enthalpy and volume are in line with

impurity related atomic-scale processes and the possibility of impurities acting as heterogeneous nucleation sites cannot be ruled out. As with the case of vacancies, study of impurity effects under a nanoindenter could be an interesting topic for future work.<sup>77</sup>

### C. Higher-dimensional heterogeneous sites

Incipient plasticity could also be initiated at many other conceivable heterogeneities in the crystal structure. Most of these would be too rare to realistically impact the statistics of incipient plasticity, including preexisting dislocations, grain boundaries, etc. For this reason we do not consider preexisting higher-dimensional defects quantitatively. However, the possibility of preexisting surface defects cannot be neglected in the present case, and asperities or ledges are well known as preferential dislocation nucleation sites.<sup>32,78,79</sup> The first displacement burst may not necessarily be associated with a dislocation nucleation event at the surface, because a semi-loop punched in from the surface would likely retract to the free surface upon unloading. These kinds of events would be subcritical and could simply superpose smoothly upon the “elastic” portion of the  $P$ - $h$  curve during loading without being detected as a burst.<sup>28</sup> However, any such subcritical dislocations injected in this manner would be natural heterogeneous sites for the initiation of a dislocation source upon further loading. For example, one can imagine that a small semicircular loop would cross slip in the complex stress field under the indenter, leading to Frank–Read source activation from the point of cross slip. This process seems plausible in light of the activation enthalpy we have extracted ( $\sim 0.3$  eV), which is close to typical values for dislocation multiplication-limited flow of metal crystals.<sup>80</sup>

It is interesting to note that the notion of subcritical dislocations has been considered previously for materials with a significant native oxide layer on the indented surface. In this case Gerberich and co-workers<sup>22</sup> explained how the development of a dislocation structure could significantly precede the displacement burst. In the present case of an oxide-free surface the situation is less clear, although the recent simulation work of Knap and Ortiz has shown that the relatively large radii of experimental nanoindenter tips may produce significant dislocation activity before the first burst point is reached.<sup>28</sup> Clearly, this kind of activity would produce “pre-existing” heterogeneous sites to facilitate a detectable event, and could well be in line with our measured activation parameters. Without some understanding of the surface ledge/asperity statistics and how these affect the development of subcritical dislocation structures, it is not obvious how our analytical approach can be adapted to cover this complex situation. However, the inclusion of an additional probability function associated with a preexisting defect density would certainly change the shape of cumulative data like those in Fig. 7, and these kinds of effects could explain why the tails of some curves do not match exactly between experiment and model.

### D. Yield stress in incipient plasticity

As discussed earlier, the broad distributions of yield loads we have measured by nanoindentation (Fig. 7) imply that for

most every experiment we have conducted, the shear stress at yield was significantly below the ideal shear strength of defect-free platinum ( $\sim 5.3$  GPa).<sup>61</sup> In this context it is also instructive to assess the athermal shear yield stress for an average volume of platinum from the experimental data, which is estimated from our statistical model as  $\tau = \varepsilon/V \approx 4.4$  GPa. This value is somewhat lower than the calculated ideal shear strength of 5.3 GPa, and although these values are both only rough approximations, this result is in line with expectations for a heterogeneous nucleation mechanism. One caveat to the present discussion pertains to our use of the maximum shear stress at every point in the crystal, rather than the maximum resolved shear stress assigned to a viable slip system. Although we have incorporated this complexity into another variation of our second-order model (not discussed here), we find that this amounts to a minor multiplicative factor on the stress components in the Hertzian field, and does not significantly impact the extracted activation parameters. In support of this, we have also conducted some experiments on platinum crystals of a different orientation [(111) as opposed to (110) as discussed herein]. These experiments yielded essentially similar activation volume, activation enthalpy, and attempt frequency as did the experiments on (110)-oriented crystals discussed above. This result is shown in Table I, and the experimental results are briefly described in Appendix B. The critical point here is that crystallography seems to play a relatively minor role in the mechanisms governing incipient plasticity during nanoindentation, in the sense that it does not affect the rate-limiting step of plastic yield.

## VII. CONCLUSION

Incipient plasticity has been studied on single crystal specimens of platinum, with particular emphasis on time and temperature dependencies of plastic yield. By performing a large number of experiments under nominally identical conditions, the activation enthalpy, activation volume, and attempt frequency for incipient plasticity have been extracted using statistical means. We have presented two complementary mathematical approaches to this problem. First, we have developed a simple analytical and graphical construction (the “first-order” model), which is suitable for routine use and loses little accuracy despite simplifying assumptions. Second, we have implemented a more rigorous numerical scheme (the “second-order” model), which captures the full complexity of the stress field beneath a nanoindentation. Using either approach, fitting these models to the experimental data gave an activation enthalpy for plastic yield during nanoindentation of the order  $\sim 0.3$  eV, and an activation volume near one atomic volume.

By adapting the second-order model, we have also explored the viability of various mechanisms for incipient plasticity that have been proposed in the literature. We conclude from this analysis that two commonly discussed mechanisms are unlikely candidates for that controlling the behavior seen in our experiments:

- Homogeneous dislocation nucleation would have far lower rate and temperature dependence than we see in our

experiments, owing to the expected larger activation volumes and energies of that process.

- Mechanisms based on vacancy migration (e.g., climb of subcritical dislocation loops) are untenable. This is not surprising in light of the very slow migration rate of vacancies at the temperatures studied, even in a steep pressure gradient beneath the indenter.

In contrast, there are many mechanisms that remain plausible in light of our analysis:

- Heterogeneous nucleation of dislocations at pre-existing point defects is possible, but may require an inflated, non-equilibrium density of vacancies.

- Activation of dislocation sources is possible if surface ledges or asperities can assist the initial formation of sub-surface subcritical dislocations.

## ACKNOWLEDGMENTS

This work was supported by the Office of Naval Research, Grant No. N00014-04-1-0669; the views expressed herein are not endorsed by the sponsor. Collaborative support of Hysitron, Inc., as well as the collaborative involvement of Dr. Andrea Hodge (Lawrence Livermore National Laboratory), are gratefully acknowledged.

## APPENDIX A: BURST STATISTICS FOR A CONSTANT SHEAR STRESS RATE

Although constant loading rate is the most common condition used in nanoindentation tests, for the evaluation of activation parameters we propose that a simpler procedure is to use a cubic loading profile such as given by Eq. (24)

$$P = At^3. \quad (\text{A1})$$

This loading function yields, via Eq. (8), a nanoindentation where the maximum shear stress beneath the indenter tip increases at a constant rate. This simplifies the mathematics of our first-order analysis quite substantially, as the time integral in Eq. (7) evaluates with significantly fewer higher-order correction terms. By combining Eqs. (8), (9), (5), and (7), and introducing Eq. (A1), the following closed-form solution is derived for the cumulative burst statistics:

$$F(t) = 1 - \exp \left\{ - \frac{3\pi\rho A^{1/3} \cdot [1 + \exp(P^{1/3}\alpha) \cdot (P^{1/3}\alpha - 1)]}{4E_R\alpha^2} \times \eta \exp\left(-\frac{\varepsilon}{kT}\right) \right\}. \quad (\text{A2})$$

Equation (A2) is analogous to Eq. (11), but with the linear loading profile replaced by the cubic one; neither of these two equations can be reduced to the other through a simple substitution, as the time dependence of the loading function influences the time integral in Eq. (7).

In order to analyze experimental data using Eq. (A2), one proceeds along the same lines developed in the text in Eqs.

(20)–(23). Equation (A2) is first recast in the form

$$\begin{aligned} & \ln \left[ \ln \left( \frac{1}{1-F(P)} \right) \right] \\ &= \alpha P^{1/3} + \ln \left\{ \frac{3\pi\rho A^{1/3} \cdot [\exp(-P^{1/3}\alpha) + P^{1/3}\alpha - 1]}{4E_R\alpha^2} \right. \\ & \quad \left. \times \eta \exp \left( -\frac{\varepsilon}{kT} \right) \right\}. \end{aligned} \quad (\text{A3})$$

The activation volume is extracted from experimental data by plotting  $\ln[\ln(1-F)^{-1}]$  vs  $P^{1/3}$ , using least-squares linear fitting to obtain the value of  $\alpha$ , and calculating  $V$  from Eq. (22). It is worth noting that this is the identical procedure used earlier with reference to constant loading rate experiments; although the loading function has changed, the same plot (Fig. 5) is used for the analysis. Comparison of Eq. (A3) with Eqs. (20) and (21) reveals that the change in loading function led to only higher-order corrections to the intercept term,  $\beta$ .

The activation enthalpy may now be extracted from the experimental data in the same way as was done with Eq. (23). For fixed values of  $F(P)$  and  $A$ , Eq. (A2) rearranges as

$$\begin{aligned} P^{1/3} = & \ln \left[ -\frac{4E_R\alpha^2 \ln[1-F(P)]}{3\pi\rho A^{1/3} \eta \cdot [\exp(-P^{1/3}\alpha) + P^{1/3}\alpha - 1]} \right] \cdot kT \\ & + \frac{\pi}{0.47} \left( \frac{3\rho}{4E_R} \right)^{2/3} \frac{\varepsilon}{V} \end{aligned} \quad (\text{A4})$$

and linear least-squares fitting as per Fig. 6 allows calculation of  $\varepsilon$ . By comparing Eq. (A4) with Eq. (23), for constant shear stress rate and constant loading rate, respectively, we again find that the change in loading function led to relatively inconsequential corrections to the displacement burst statistics. In this case the slope,  $\gamma$ , is comprised of different terms, but these are negligible in the extraction of  $\varepsilon$ .

#### APPENDIX B: INCIPIENT PLASTICITY ON (111)-ORIENTED PLATINUM

All of the experimental data presented in the text were acquired on (110)-oriented platinum; in order to expand the discussion to other crystal orientations we have also performed a limited number of experiments on single crystals of (111) orientation. This material was acquired from the same source and procedures for specimen preparation and testing were identical, except that for the (111)-oriented specimens only six different combinations of loading rate and temperature were explored. For each test condition between 63 and 162 indentations were performed, and the load at the first displacement burst was identified. The data are collected in Fig. 9 by test temperature, plotted as cumulative burst distributions. The results are qualitatively similar to those presented for the (110) surface, and also exhibit similar quantitative features.

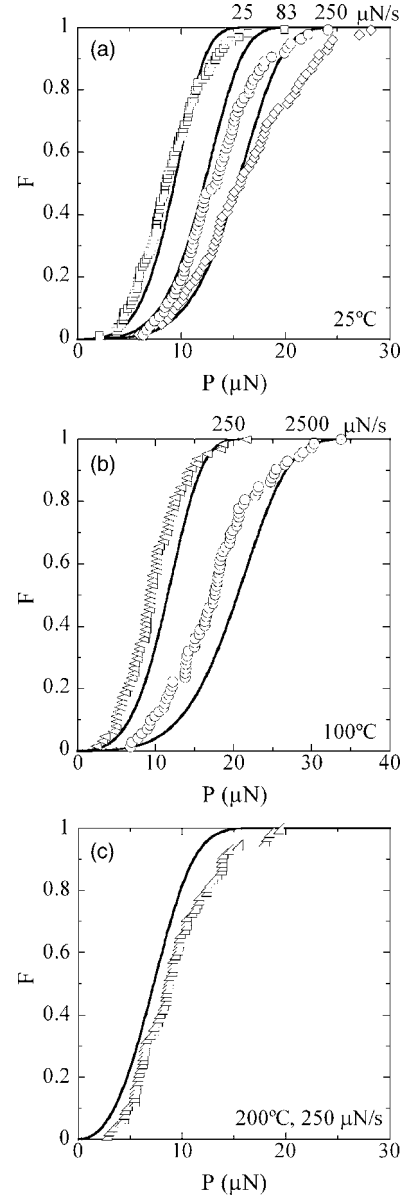


FIG. 9. Experimental data collected for constant loading rate indentations on (111)-oriented platinum, plotted as cumulative fractions of the load  $P$  at the first displacement burst. Fitting this data with the second-order analysis with a shear bias according to Eq. (18) yields the solid lines, and the activation parameters resulting from this fit are similar to those obtained from analysis of the data for (110)-oriented platinum in Fig. 7 (cf. Table I).

Using the second-order analysis developed in the text, these data for (111)-oriented platinum have been analyzed to extract the activation parameters. This analysis accounts for shear bias occurring at any position beneath the indenter, inclusive of the full variation of the maximum shear stress field by using Eq. (18) as the bias in Eq. (19). The results of this fitting procedure are shown by the solid lines in Fig. 9, and match the form of the experimental data quite well. The extracted activation parameters from this fit are collected in the bottom row of Table I.

- \*Author to whom correspondence should be addressed. Electronic mail: schuh@mit.edu
- <sup>1</sup>C. A. Schuh and A. C. Lund, *J. Mater. Res.* **19**, 2152 (2004).
  - <sup>2</sup>Y. L. Chiu and A. H. W. Ngan, *Acta Mater.* **50**, 2677 (2002).
  - <sup>3</sup>J. D. Kiely and J. E. Houston, *Phys. Rev. B* **57**, 12588 (1998).
  - <sup>4</sup>N. I. Tymiak, A. Daugela, T. J. Wyrobek, and O. L. Warren, *Acta Mater.* **52**, 553 (2004).
  - <sup>5</sup>D. Lorenz, A. Zeckzer, U. Hilpert, P. Grau, H. Johansen, and H. S. Leipner, *Phys. Rev. B* **67**, 172101 (2003).
  - <sup>6</sup>S. A. Syed-Asif and J. B. Pethica, *Philos. Mag. A* **76**, 1105 (1997).
  - <sup>7</sup>S. G. Corcoran, R. J. Colton, E. T. Lilleodden, and W. W. Gerberich, *Phys. Rev. B* **55**, R16057 (1997).
  - <sup>8</sup>D. F. Bahr, D. E. Kramer, and W. W. Gerberich, *Acta Mater.* **46**, 3605 (1998).
  - <sup>9</sup>W. W. Gerberich, S. K. Venkataraman, H. Huang, S. E. Harvey, and D. L. Kohlstedt, *Acta Metall. Mater.* **43**, 1569 (1995).
  - <sup>10</sup>Y. L. Chiu and A. H. W. Ngan, *Acta Mater.* **50**, 1599 (2002).
  - <sup>11</sup>W. Wang, C. B. Jiang, and K. Lu, *Acta Mater.* **51**, 6169 (2003).
  - <sup>12</sup>T. F. Page, W. C. Oliver, and C. J. McHargue, *J. Mater. Res.* **7**, 450 (1992).
  - <sup>13</sup>H. Bei, Z. P. Lu, and E. P. George, *Phys. Rev. Lett.* **93**, 125504 (2004).
  - <sup>14</sup>S. K. Venkataraman, D. L. Kohlstedt, and W. W. Gerberich, *J. Mater. Res.* **8**, 685 (1993).
  - <sup>15</sup>R. C. Thomas, J. E. Houston, T. A. Michalske, and R. M. Crooks, *Science* **259**, 1883 (1993).
  - <sup>16</sup>T. A. Michalske and J. E. Houston, *Acta Mater.* **46**, 391 (1998).
  - <sup>17</sup>L. Zuo, A. H. W. Ngan, and G. P. Zheng, *Phys. Rev. Lett.* **94**, 095501 (2005).
  - <sup>18</sup>C. L. Kelchner, S. J. Plimpton, and J. C. Hamilton, *Phys. Rev. B* **58**, 11085 (1998).
  - <sup>19</sup>R. E. Miller, L. E. Shilkrot, and W. A. Curtin, *Acta Mater.* **52**, 271 (2004).
  - <sup>20</sup>E. T. Lilleodden, J. A. Zimmerman, S. M. Foiles, and W. D. Nix, *J. Mech. Phys. Solids* **51**, 901 (2003).
  - <sup>21</sup>M. Pang, D. F. Bahr, and K. G. Lynn, *Appl. Phys. Lett.* **82**, 1200 (2003).
  - <sup>22</sup>W. W. Gerberich, J. C. Nelson, E. T. Lilleodden, P. Anderson, and J. T. Wyrobek, *Acta Mater.* **44**, 3585 (1996).
  - <sup>23</sup>W. W. Gerberich, N. I. Tymiak, D. E. Kramer, A. Daugela, J. Jungk, and M. Li, *Philos. Mag. A* **82**, 3349 (2002).
  - <sup>24</sup>A. Gouldstone, H. J. Koh, K. Y. Zeng, A. E. Giannakopoulos, and S. Suresh, *Acta Mater.* **48**, 2277 (2000).
  - <sup>25</sup>S. Suresh, T. G. Nieh, and B. W. Choi, *Scr. Mater.* **41**, 951 (1999).
  - <sup>26</sup>K. J. Van Vliet, J. Li, T. Zhu, S. Yip, and S. Suresh, *Phys. Rev. B* **67**, 104105 (2003).
  - <sup>27</sup>A. Gannepalli and S. K. Mallapragada, *Phys. Rev. B* **66**, 104103 (2002).
  - <sup>28</sup>J. Knap and M. Ortiz, *Phys. Rev. Lett.* **90**, 226102 (2003).
  - <sup>29</sup>D. F. Bahr, D. E. Wilson, and D. A. Crowson, *J. Mater. Res.* **14**, 2269 (1999).
  - <sup>30</sup>A. M. Minor, E. T. Lilleodden, M. Jin, E. A. Stach, D. C. Chrzan, and J. W. Morris, *Philos. Mag.* **85**, 323 (2005).
  - <sup>31</sup>A. M. Minor, E. T. Lilleodden, E. A. Stach, and J. W. Morris, *J. Mater. Res.* **19**, 176 (2004).
  - <sup>32</sup>J. P. Hirth and J. Lothe, *Theory of Dislocations* (Wiley, New York, 1982).
  - <sup>33</sup>R. E. Miller and A. Acharya, *J. Mech. Phys. Solids* **52**, 1507 (2004).
  - <sup>34</sup>D. E. Kramer, K. B. Yoder, and W. W. Gerberich, *Philos. Mag. A* **81**, 2033 (2001).
  - <sup>35</sup>A. C. Lund, A. M. Hodge, and C. A. Schuh, *Appl. Phys. Lett.* **85**, 1362 (2004).
  - <sup>36</sup>C. A. Schuh, J. K. Mason, and A. C. Lund, *Nat. Mater.* **4**, 617 (2005).
  - <sup>37</sup>A. B. Mann and J. B. Pethica, *Appl. Phys. Lett.* **69**, 907 (1996).
  - <sup>38</sup>A. B. Mann and J. B. Pethica, *Philos. Mag. A* **79**, 577 (1999).
  - <sup>39</sup>C. A. Schuh, A. C. Lund, and T. G. Nieh, *Acta Mater.* **52**, 5879 (2004).
  - <sup>40</sup>C. A. Schuh, C. E. Packard, and A. C. Lund, *J. Mater. Res.* in print (2006).
  - <sup>41</sup>R. Farraro and R. B. McLellan, *Metall. Trans. A* **8**, 1563 (1977).
  - <sup>42</sup>S. M. Collard and R. B. McLellan, *Acta Metall. Mater.* **40**, 699 (1992).
  - <sup>43</sup>M. Werner, S. Klose, F. Szucs, C. Moelle, H. J. Fecht, C. Johnston, P. R. Chalker, and I. M. Buckley Golder, *Diamond Relat. Mater.* **6**, 344 (1997).
  - <sup>44</sup>F. Szucs, M. Werner, R. S. Sussmann, C. S. J. Pickles, and H. J. Fecht, *J. Appl. Phys.* **86**, 6010 (1999).
  - <sup>45</sup>G. B. Brook, in *Smithell's Metals Reference Book*, edited by E. A. Brandes and G. B. Brook (Butterworth-Heinemann, Oxford, UK, 1999).
  - <sup>46</sup>B. Bhushan, in *Handbook of Micro/Nano Tribology*, edited by B. Bhushan (CRC, Boca Raton, FL, 1999), p. 433.
  - <sup>47</sup>B. Luan and M. Robbins, *Nature (London)* **435**, 929 (2005).
  - <sup>48</sup>K. L. Johnson, *Contact Mechanics* (Cambridge University Press, Cambridge, 1985).
  - <sup>49</sup>A. C. Fischer-Cripps, *Introduction to Contact Mechanics* (Springer, New York, 2000).
  - <sup>50</sup>M. Fago, R. L. Hayes, E. A. Carter, and M. Ortiz, *Phys. Rev. B* **70**, 100102 (2004).
  - <sup>51</sup>J. Li, K. J. Van-Vliet, T. Zhu, S. Yip, and S. Suresh, *Nature (London)* **418**, 307 (2002).
  - <sup>52</sup>T. Zhu, J. Li, K. J. Van-Vliet, S. Ogata, S. Yip, and S. Suresh, *J. Mech. Phys. Solids* **52**, 691 (2004).
  - <sup>53</sup>O. R. de la Fuente, J. A. Zimmerman, M. A. Gonzalez, J. de la Figuera, J. C. Hamilton, W. W. Pai, and J. M. Rojo, *Phys. Rev. Lett.* **88**, 036101 (2002).
  - <sup>54</sup>L. Dupuy, E. Tadmor, R. Miller, and R. Phillips, *Phys. Rev. Lett.* **95**, 060202 (2005).
  - <sup>55</sup>M. Khantha, D. Pope, and V. Vitek, *Phys. Rev. Lett.* **73**, 684 (1994).
  - <sup>56</sup>M. Khantha and V. Vitek, *Acta Mater.* **45**, 4675 (1997).
  - <sup>57</sup>H. Wollenberger, in *Physical Metallurgy*, edited by R. W. Cahn and P. Haasen (North-Holland, Amsterdam, 1996).
  - <sup>58</sup>G. Xu and A. Argon, *Philos. Mag. Lett.* **80**, 605 (2000).
  - <sup>59</sup>G. Xu and A. Argon, *Mater. Sci. Eng., A* **319**, 144 (2001).
  - <sup>60</sup>T. Zhu, J. Li, and S. Yip, *Phys. Rev. Lett.* **93**, 025503 (2004).
  - <sup>61</sup>J. Pokluda, M. Cerny, P. Sandera, and M. Sob, *J. Comput.-Aided Mater. Des.* **11**, 1 (2004).
  - <sup>62</sup>M. Khantha, D. Pope, and V. Vitek, *Acta Mater.* **45**, 4687 (1997).
  - <sup>63</sup>M. Khantha, D. Pope, and V. Vitek, *Mater. Sci. Eng., A* **234**, 629 (1997).
  - <sup>64</sup>Y. Q. Sun, P. M. Hazzledine, and P. B. Hirsch, *Phys. Rev. Lett.* **88**, 065503 (2002).
  - <sup>65</sup>J. Jung, *Philos. Mag. A* **43**, 1057 (1981).
  - <sup>66</sup>A. C. Lund and C. A. Schuh, *Acta Mater.* **53**, 3193 (2005).
  - <sup>67</sup>S. Cheng, J. A. Spencer, and W. W. Milligan, *Acta Mater.* **51**,

- 4505 (2003).
- <sup>68</sup>P. C. Wo, L. Zuo, and A. H. W. Ngan, *J. Mater. Res.* **20**, 489 (2005).
- <sup>69</sup>R. D. Boyer and S. Yip, unpublished research, MIT, Cambridge, MA (2005).
- <sup>70</sup>Y. I. Golovin, A. I. Tyurin, and B. Y. Farber, *Philos. Mag. A* **82**, 1857 (2002).
- <sup>71</sup>Y. Golovin, A. Tyurin, and B. Farber, *J. Mater. Res.* **37**, 895 (2002).
- <sup>72</sup>B. Y. Farber, V. I. Orlov, and A. H. Heuer, *Phys. Status Solidi A* **166**, 115 (1998).
- <sup>73</sup>B. Y. Farber, V. I. Orlov, V. I. Nikitenko, and A. H. Heuer, *Philos. Mag. A* **78**, 671 (1998).
- <sup>74</sup>P. C. Wo and A. H. W. Ngan, *Philos. Mag.* **84**, 3145 (2004).
- <sup>75</sup>F. Seitz, *Phys. Rev.* **79**, 890 (1950).
- <sup>76</sup>F. R. N. Nabarro, *Theory of Crystal Dislocations* (Dover, New York, 1987).
- <sup>77</sup>D. F. Bahr and G. Vasquez, *J. Mater. Res.* **20**, 1947 (2005).
- <sup>78</sup>J. A. Zimmerman, C. L. Kelchner, P. A. Klein, J. C. Hamilton, and S. M. Foiles, *Phys. Rev. Lett.* **87**, 165507 (2001).
- <sup>79</sup>A. Gouldstone, K. J. Van-Vliet, and S. Suresh, *Nature* (London) **411**, 656 (2001).
- <sup>80</sup>H. Conrad, in *High Strength Materials*, edited by V. F. Zackay (Wiley, New York, 1965), p. 436.